Internal fatigue crack propagation in a Ti-6Al-4V alloy: An in situ study

Arnaud Junet [a], Alexandre Messager [b], Arnaud Weck [c,d,e], Yves Nadot [f], Xavier Boulnat [a], Jean-Yves Buffiere [a,*]

[a] Université de Lyon, INSA-Lyon, MATEIS, CNRS UMR 5510, F-69621 Villeurbanne, France
[b] Arts et Metiers ParisTech, I2M Bordeaux, CNRS, Université de Bordeaux, Esplanade des Arts et Metiers, F-33405 Talence, France
[c] Department of Mechanical Engineering, University of Ottawa, 150 Louis Pasteur, Ottawa, ON, K1N 6N5, Canada
[d] Centre for Research in Photonics, University of Ottawa, 25 Templeton, Ottawa, ON, K1N 6N5, Canada
[e] Department of Physics, University of Ottawa, 150 Louis-Pasteur, Ottawa, ON, K1N 6N5, Canada
[f] Institut PRPIME ISAE-ENSMA, CNRS, Univervisté de Poitiers, Futuroscope Chasseneuil, Cedex, France

Keywords:
Internal fatigue cracks
Three-dimensional tomography
Synchrotron radiation
Titanium alloys
Small fatigue cracks

A B S T R A C T

Fatigue specimens of a Ti-6Al-4V alloy containing internal artificial defects with controlled and reproducible size and shape have been produced. These defects systematically led to the initiation of a fatigue crack which propagation has been monitored in situ by synchrotron X-ray tomography during R=0.1 uniaxial fatigue tests at 20 Hz. The crack growth curves of the internal cracks have been obtained for 6 samples. Ex situ fatigue tests have been performed on samples submitted to a supplementary heat treatment or containing a defect put into contact with air. The results obtained tend to support the fact that internal fatigue cracks grow from the notch in a vacuum environment. On the fracture surfaces of samples containing an artificial defect not connected to air, two regions have been observed. They correspond to the Rough Area and the Fish Eye regions observed for internal cracks initiated from natural defects. The transition between those two regions takes place when the plastic radius size is equivalent to the grain size.

1. Introduction

Titanium alloys are one of the key structural materials used for the production of aerospace engines. Even if the reasons for using this class of material are multiple (low density, excellent corrosion resistance etc.) their outstanding fatigue strength has played a central role in their use. As a result, a large amount of literature has been devoted to the topic of the fatigue properties of Ti alloys. In the vast majority of cases, in high cycle fatigue, fatigue cracks initiate *at* and develop *from* surfaces (or immediate sub-surface regions) where cyclic plasticity is easier. This has some very important practical consequences as critical components in plane engines can be inspected visually at regular intervals during maintenance to detect possible damage. In some cases, however, fatigue cracks can remain invisible to such inspections because they develop internally. This problem, although rare, can have some dramatic consequences as shown by two recent accidents [1,2].

If the literature on surface fatigue cracks initiation and propagation in metallic alloys is more than abundant, the amount of experimental data available on internal fatigue crack growth is much more limited. One recent special issue of the journal *Fatigue & Fracture of Engineering Materials and Structures* has been devoted to the topic of *Internal Fatigue Cracks* but no *direct* observation of internal crack propagation was shown when the issue appeared (2017). Since then, with the development of tomographic imaging techniques, 3D images of propagating fatigue cracks have become more common (see [3] for a list)). While getting quantitative information on the way fatigue cracks propagate in the bulk of optically opaque materials brings new and interesting information for the design of fatigue sensitive components, it has rarely focused, so far, on cases where *both* crack initiation and propagation happen in the bulk [4–6]. One reason of such limited data is that internal crack initiation is a stochastic process which reduces the number of successful experiments (another one is that, data analysis of tomographic data, when available, takes time).

In a recent work [7] we have reported the development of a method for introducing controlled internal defects within metallic fatigue samples without disturbing the local microstructure around the defect. By using synchrotron X ray tomography we showed that it was possible to analyze fatigue crack propagation from those defects and to extract quantitative data on the propagation of internal fatigue cracks. The study presented here builds on this preliminary work.

A systematic analysis of crack propagation from internal defects introduced in a Ti-4Al-6V alloy is carried out using synchrotron tomography during in situ fatigue tests. Propagation curves of internal fatigue

* Corresponding author.
E-mail address: jean-yves.buffiere@insa-lyon.fr (J.-Y. Buffiere).

https://doi.org/10.1016/j.ijfatigue.2022.107450

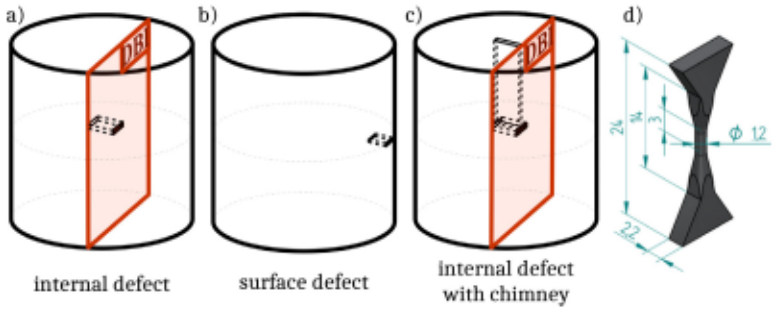

Fig. 1. Schematic drawing of the different location of defects within the fatigue specimens used for *in situ* and *ex situ* tests. (a), (b), (c) enlargement of the central gauge length, (d) geometry and size of the specimens.

Table 1
Tensile properties of Ti-6Al-4V sheets, before and after diffusion bonding (DB).

Sheet	Tensile strength (MPa)	0.2% proof stress (MPa)	Elongation (%)
Sheet 1 (containing the notch)	1026	935	12
Sheet 2	944	855	13
DB sheets	1070	915	14

cracks have been obtained for various conditions of environment in the internal defects. The level on vacuum reached in the defects has been assessed thanks to complementary experiments. The typical features of internal crack propagation (Fish Eye and Rough Area regions [8]) have been observed and analyzed quantitatively for the first time directly based on internal 3D crack fronts.

2. Materials and methods

2.1. Samples with internal controlled defects

The studied material was a Ti-6Al-4V titanium alloy composed of 94% α phase. The method used to produce the fatigue samples with controlled internal defects is briefly summarized in what follows; more details can be found in [7].

The notches were created in one sheet by translating it under the stationary beam of a Yb:KGW femtosecond laser in a back and forth motion (6 times) at the speed of 0.1 mm/s. This process generated 200 µm wide, 200 µm deep and 20 µm thick grooves. The sheets were then placed in an ultrasonic bath for 5 min to remove debris from the laser ablation process. The sheet containing the notch and the un-notched one have been welded by Spark Plasma Sintering (SPS). One of them contained a notch-like defect machined by femtosecond laser (Fig. 1). The textures of the two sheets have been analyzed using EBSD. The results are shown in Fig. 2 where it can be seen that both sheets had a similar texture with a slightly larger fraction of basal planes perpendicular to the rolling direction (which was also the loading direction in this work) in the sheet containing the notch [7].

The welding time and temperature were chosen so as to not alter the initial microstructure of the material. The average grain size d_g in the fatigue samples, determined form EBSD measurements, based on a grain area histogram [9] was found equal to 4.4 µm. The mechanical properties of the material before and after bonding are listed in Table 1.

Dog bone fatigue samples (geometry in Fig. 1) were extracted from the welded sheets by electro discharge machining. Three types of samples have been used. The first type, hereafter labeled *internal*, contained the internal notch in the middle of the cross section located at the center of the specimens gauge length which, after manual mechanical polishing, had a circular section (diameter ~ 1.2 mm). The second type, labeled hereafter *surface*, contained a notch at the surface. Finally, some

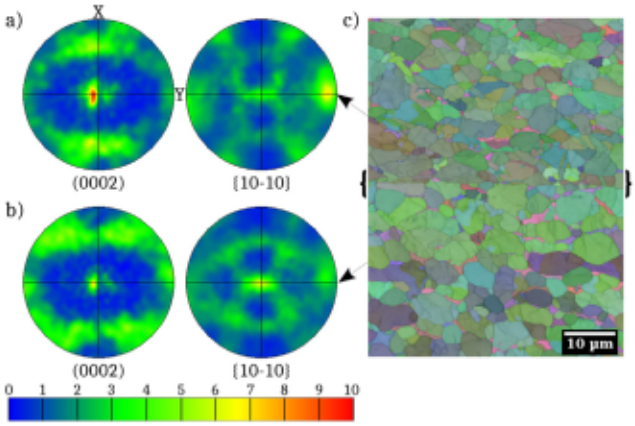

Fig. 2. EBSD maps of the microstructure of the two different sheets used after diffusion bonding. The bonding interface is indicated by the {} symbols. The texture is similar in both sheets with a slightly larger number of basal planes perpendicular to the rolling direction (the loading direction of the fatigue tests) in the sheets where the laser notch is machined.

specimens, labeled *chimney* hereafter, contained the notch as well as a central hole also produced by the femtolaser before SPS bonding; this hole enabled to put the internal notch into contact with the laboratory air. Those three types of samples are schematically shown in Fig. 1.

The bonding of the sheets has been performed either using primary vacuum in the SPS chamber (samples labeled *vacuum* hereafter) or an inert Argon gas (samples labeled *argon* hereafter) [7]. Finally, one sample (labeled hereafter *ThT*) containing an internal defect has been submitted to a supplementary heat treatment before cycling in order to evacuate the notch from possible traces of oxygen: 5 h at 750 °C under secondary vacuum (5.10^{-2} Pa) followed by slow air cooling.

2.2. Crcak propagation fatigue tests

Uni-axial fatigue tests have been performed at Institut P' on macroscopic SENT samples [9] extracted from the sheets previously submitted to the same thermal treatment than the one used in SPS during bonding. Those tests have been carried out at 30 Hz with a load ratio of 0.1 in air or under vacuum (10^{-3} Pa). The formula for computing the values of the Stress Intensity Factor (SIF) is taken from [10]:

$$\Delta K_{sent} = \Delta P \frac{\sqrt{\pi a_s}}{BW}\left[1.12 - 0.23\left(\frac{a_s}{W}\right) + 10.55\left(\frac{a_s}{W}\right)^2 - 21.71\left(\frac{a_s}{W}\right)^3 + 30.38\left(\frac{a_s}{W}\right)^4\right] \quad (1)$$

Where ΔP is the intra cycle load variation ($\Delta P = P_{max} - P_{min}$), a_s the crack length, B and W the sample thickness and width, respectively. Cracks have been initiated from the notch by cycling above ΔK_{th} and the test were performed at decreasing values of SIF. The crack length

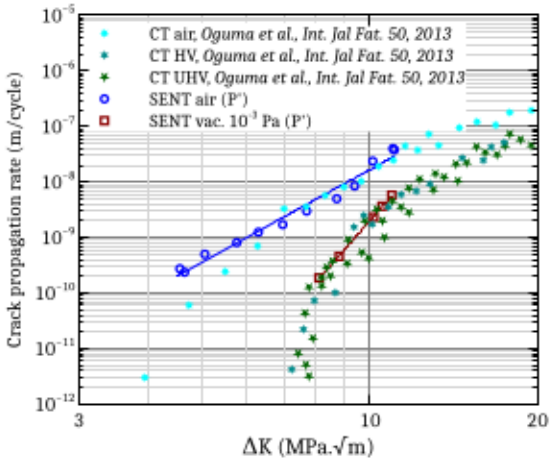

Fig. 3. Crack propagation curves obtained by SENT tests on the Ti sheets in vacuum and in air. Prior to testing the sheets have been submitted to a heat treatment corresponding to the welding cycle in the SPS.

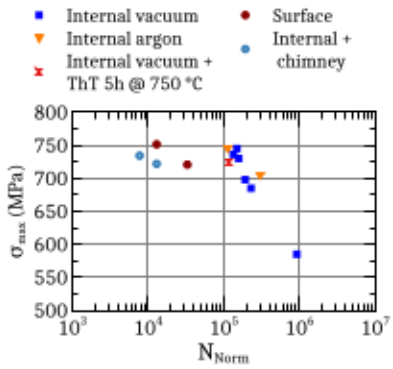

Fig. 4. S–N curves obtained from the ex situ fatigue tests. The numbers of cycles to failure are normalised by the fatigue life of the sample with the smallest artificial defect as explained in Appendix A.

is the average of the values measured optically on both sides of the samples. Two samples have been tested one for each environment. The da/dN curves are plotted using nominal values, no crack closure measurement has been performed.

One part of the dog bone samples have been submitted to *in situ* uniaxial fatigue tests monitored by synchrotron X-ray tomography on ID19 beamline of ESRF using a dedicated fatigue rig. The other part has been cycled in the laboratory using the same machine. A cycling frequency of 20 Hz with a load ratio R equal to 0.1 has been used in both cases. The maximum stress level was chosen to obtain a lifetime of a few hundred thousand cycles in order to perform between 5 and 10 tests during a synchrotron campaign. Under these conditions, the initiation of a fatigue crack occurred rapidly (less than 10% of the fatigue life) and was systematically located at the artificial defect. All tests have been performed at room temperature in ambient air.

In order to increase the visibility of the cracks, Tomography scans of the sample were recorded under maximum load (scan duration ~ 5 min) around the notch before cycling and then regularly during the life of the sample [9]. The details of the imaging conditions are given in [7]. The voxel size of the reconstructed Three Dimensional (3D) image is equal to 0.7 µm. The spatial resolution is of the order of twice this value.

The fracture surfaces of the samples cycled to fracture in the laboratory have been analyzed (i) at a macroscale using a confocal optical microscope (JYFEL Hirox RH-2000) and (ii) at a local scale with a Scanning Electron Microscope (SEM) Zeiss Supra 55 VP operated at 20 kV in Secondary Electron (SE) mode.

3. Results

3.1. Long crack behavior

The results of the SENT tests are shown in Fig. 3. As expected, in vacuum, lower crack growth rates are measured compared to air. A good agreement is found between our data and that obtained by Oguma and Nakamura on a similar alloy [11]. The following Paris parameters have been obtained:

$$(da/dN)_{air} = 5.148.10^{-14}\Delta K^{5.51}(\text{m/cycle}) \quad (2)$$

for air and

$$(da/dN_{vac}) = 7.504.10^{-21}\Delta K^{11.43}(\text{m/cycle}) \quad (3)$$

for vacuum.

3.2. S–N curves

Fig. 4 shows the fatigue curves obtained with the samples cycled in the laboratory with the small in situ rig. For the samples with an internal notch it was verified using tomography that crack initiation is very rapid (less than 10% of the total life). Therefore, the fatigue lives showed on the figure for samples with such a notch correspond, with a good approximation, to propagation. In this case, it is well known that if the final crack length a_f before fracture has a negligible influence on the fatigue life, this is not true for the value of the initial crack length a_i. For samples with an internal defect, a_i is of the order of the notch size. The latter can vary between samples; smaller notches leading to longer fatigue lives. Therefore, in order to improve the comparison between samples, the number of cycles shown on Fig. 4 has been normalized using the number of cycles obtained for the sample with the smallest notch (see Appendix A for details). When this is done it appears that the fatigue life of samples with an internal notch welded in vacuum is similar to that of the samples produced using argon or the one submitted to the supplementary heat treatment. On the contrary, samples with a notch into contact with air, either because it is at the surface or because of the presence of the chimney, have a fatigue life which is nearly one order of magnitude smaller.

3.3. Propagation of internal cracks

The list of sample studied by tomography is given in Table 2.

The propagation of the fatigue cracks from the internal defects has been obtained from the tomography images recorded during the in situ fatigue tests at the synchrotron. As the cracks grow in mode I from the notch [7], as a first approach, a two dimensional (2D) approach on planes perpendicular to the loading direction is adopted. The procedure for extracting the successive crack fronts is detailed in Appendix B which also gives an estimation of the uncertainty level of the data. As shown in [7] and also on Fig. 10, the successive shapes of the crack fronts rapidly tend towards a circular shape. Therefore the value of the stress intensity factor was assumed to be constant along the crack front and was calculated using Murakami's formula [12]:

$$\Delta K = \kappa\sigma_{max}(1-R)\sqrt{\pi\sqrt{\text{area}}} \quad (4)$$

where κ is equal to 0.5 for internal cracks and 0.65 for surface cracks and R the stress ratio. The parameter *area* is the projected area of the crack onto the plane perpendicular to the loading axis; it is also used to compute an equivalent crack size a_{eq} which is a very good average of the different crack growth rates all the front [7]:

$$a_{eq} = \sqrt{\frac{\text{area}}{\pi}} \quad (5)$$

Table 2
Summary of the in situ fatigue tests conditions and results.

Specimen	SPS conditions	Maximum stress (MPa)	Fatigue life ($\times 10^3$ cycles)
A7 (surface)	Primary Vacuum (PV) ~ 100 Pa	320	87
A4 (internal)	PV	435	150
A2 (internal)	PV	530	45
A3 (internal)	PV	430	415[a]
C2 (internal Ar)	PV + Argon injection before DB (Ar ≥ 99.99%)	455	718[a]
C3 (internal Ar)	PV + Argon injection before DB (Ar ≥ 99.99%)	443	980[a]

[a]Broken samples.

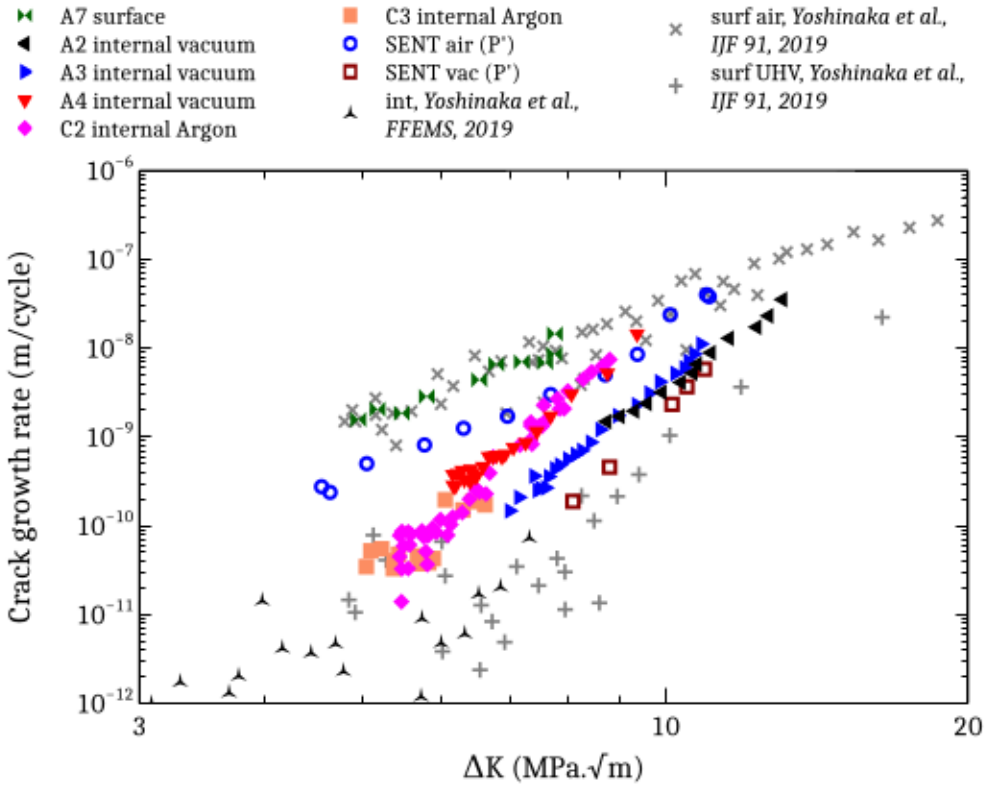

Fig. 5. Propagation curves obtained with the samples with artificial deflects, compared with literature data and with the SENT tests performed in this work.

The uncertainty induced by this data processing has been evaluated from estimation of the error on the crack front position, the load and the sample section. The detail of the calculation and its result for one sample is shown in Appendix B. The uncertainty level is larger for the ΔK values than for the (da/dN) values except when the crack size is small but, overall, remains small enough to draw conclusions.

All the propagation data have been compiled on Fig. 5 where some tendencies clearly appear. The sample with a crack growing in air from a surface notch (A7) exhibits the highest growth rate in good agreement with the SENT curve recorded in air as well as with the literature data, when uncertainty is taken into account. Two specimens (A3 and A2) have propagation curves close to long crack data recorded in vacuum. Three specimens (A4, C3, C2) have propagation curves slightly above but remain below the data recorded in air.

3.4. Fracture surface analysis

The fracture surfaces of the samples containing an internal crack have first been observed using confocal microscopy. One typical example is shown in Fig. 6 which shows the starting notch in dark with a square shape in the center of the sample cross section. Surrounding this notch, the light gray disk corresponding to the propagation of the internal crack in the so-called fish eye region can clearly be distinguished. A darker region (underlined by a white line in Fig. 6c) approximately circular and surrounding the starting notch is also visible. Those observations have been consistently made for all broken samples.

At a more local scale, SEM observations show that the initiation mechanisms are similar in air or under vacuum (see Fig. 7): facets are formed at the edge of the defect by a quasi-cleavage mechanism [13] in the sheet where the notch was machined. In Fig. 7(d), four zones have been clearly identified. The first shows cleaved grains. A second zone shows a transition between the two mechanisms involved, the cleavage zone gives way to a quasi-cleaved zone (zone 3 on the Fig. 7(d)). Finally the fourth zone represents the actual propagation of the fatigue crack.

From this narrow region, propagation occurs by different mechanisms depending on the environment encountered by the crack tip. For the crack under air (samples with a chimney) the fracture surface appears "chaotic" and sharp edges are visible. Striations (indicated by

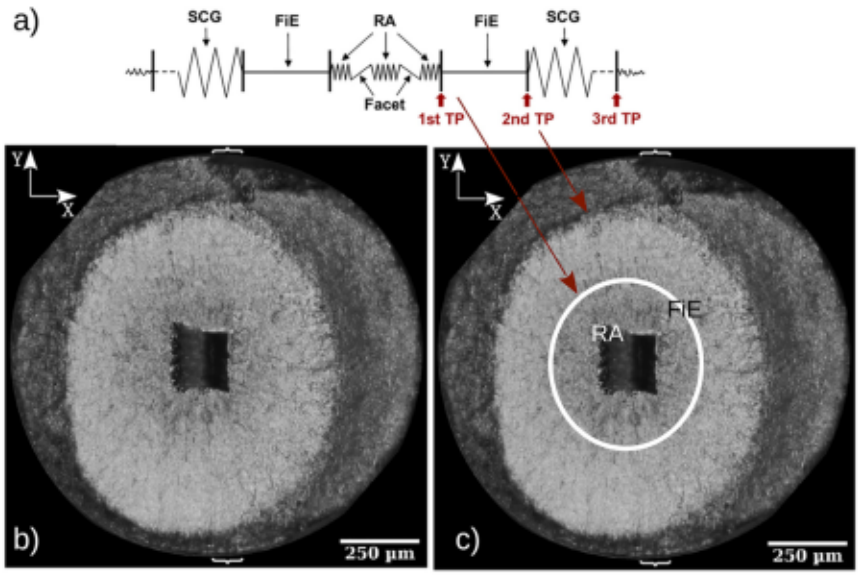

Fig. 6. (a) Schematic description of the different regions surrounding the crack initiation site (natural crack) in a Ti alloy as proposed by Hong and Sun [8]. (b) and (c) typical optical micrographs showing the initiating notch in the center, the Rough Area (RA) and the Fish Eye (FiE) regions.

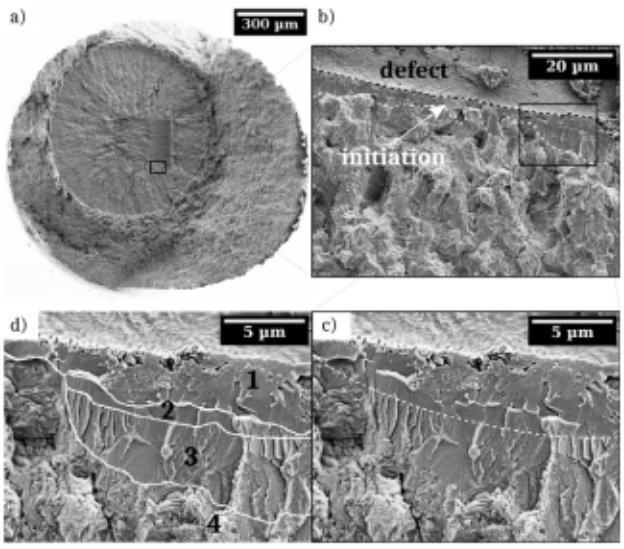

Fig. 7. Fractography of sample C2. (a) Global view. (b) Zoom on the crack initiation site. (c) and (d) Zoom on the initiation region showing the evolution of the fracture surface from some cleavage facets at the edge of the artificial defect (zone 1) to a rough morphology characteristic of propagation under vacuum (zone 4) with a transition zone in between (zone 2 and 3) with some quasi cleavage mechanisms.

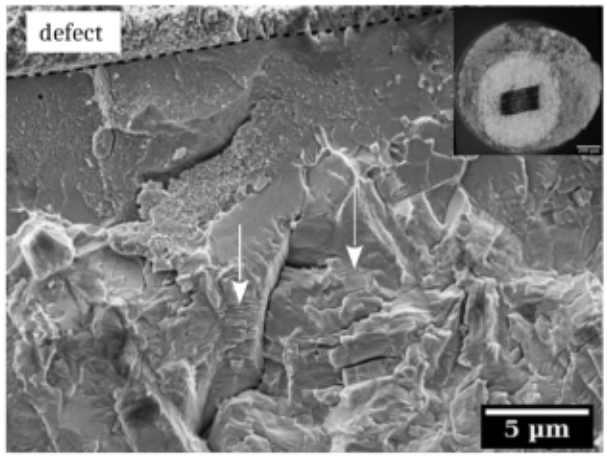

Fig. 8. Fracture surface of a sample with a chimney. The arrows point at marks which could be striations typical of crack propagation in air.

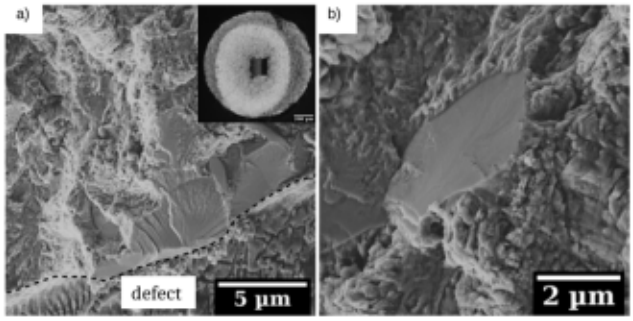

Fig. 9. (a) Fracture surface of a sample with an internal defect; the granular region ahead of the facets corresponding to crack initiation is typical of crack propagating in vacuum (b) Magnified view of a facet surrounded by granular region.

arrows in Fig. 8) can also be observed in the early stages of propagation (~ 10 µm from the notch edge). For cracks propagating in vacuum, after initiation, the fracture surface is also quite chaotic but the sharp edges have disappeared and extended very fine "granular" regions are visible. In the darker zone encircled by a white line on Fig. 6, where the value of the SIF at the crack tip is relatively low, crystallographic propagation facets can also be observed as shown in the zoomed region of Fig. 9(b) where such a facet appears surrounded by granular zones.

4. Discussion

4.1. Crack initiation from the notch

The fractographic observations of facets close to the artificial notch and away from it are in very good agreement with those of Pilchak and Williams, Uta et al. and Sinha et al. [14–16]. One can therefore reasonably assume that their analysis, which is based on EBSD and tilt orientation, remain valid in our case. These authors distinguish initiation and propagation facets. Initiation facets correspond to basal

planes (within a few degrees). Once initiated the short crack propagate in the neighboring grains creating a networks of "rivers" resembling the veins of a leaf. Those lines correspond to the junction between basal planes within the neighboring grains as explained in detail by Pilchak et al. [17] in the case of a cast Ti-6Al-4V alloy that underwent hot isostatic pressing (HIP) prior to testing.

The fact that crack initiation occurs preferentially within the sheet receiving the defect can be explained by the crystallographic texture of this sheet which presents a larger proportion of basal planes perpendicular to the direction of solicitation of the specimens. This observation is supported by initiation models and crystal plasticity (CP) simulations developed by different authors [18–21].

Dunne et al. developed a CP model [20,21] that is based on the model proposed by *Evans and Bache* [19]. Crack initiation occurs when the stress normal to the basal plane within a grain is larger than a critical "cleavage" stress, evaluated at 1200 MPa by *Jones and Hutchinson* in the case of HCP titanium [22]. CP calculations performed on a real microstructure (based on an EBSD map) showed an excellent agreement with the experimental data. Under these simulation conditions, it has been shown that the development of a basal facet occurs very rapidly during loading cycles.

CP calculations by the same authors showed that one of the most favorable conditions for fatigue dwell initiation was to have, as named by Dunne et al., a microstructure qualified as "rogue grain microstructure": a "weak" grain oriented with its $\vec{c}$ axis almost perpendicular to the direction of tension and a prismatic plane at 70° to the axis of tension beside a "strong" grain oriented parallel to the axis of tension.

In our case, it is the defect that concentrates the stresses and not a slip band at the level of a weak grain. Initiation occurs at the notch edge (which is the sharper part of the notch as shown from 3D images [9]) most probably by cracking of basal planes.

4.2. Crack propagation from the internal notch

To the best of the author's knowledge, the only experimental evidence of internal crack growth at room temperature in a Ti alloy is from a Japanese group who has also performed tomography synchrotron experiments (ex situ in that case) [6]. This data is shown on Fig. 5. In the literature it has been assumed that internal fatigue cracks propagate under vacuum conditions. The long crack data obtained from the SENT experiments in vacuum and in air are in very good agreement with other work on the same alloy using CT specimens [11] (not shown on the curve for the sake of clarity). This data fits reasonably well (when the uncertainty level is taken into account) with the crack growth rate measured for the cracks emanating from the notch.

The plastic radius, of our internal cracks has been evaluated using the following formula [23]:

$$r_p = \frac{1}{6\pi}\left(\frac{K_{max}}{\sigma_y}\right)^2 \tag{6}$$

Where σ_y is the yield stress of the diffusion bonded material. For all the samples investigated in this work, and listed in Table 2 r_p was found to vary from 5 μm to 15 μm between the beginning and the end of propagation shown in Fig. 5 *i.e.* from 1 to 3 times the grain size. For a crack to be considered long, its size must be at least fifty times the size of its plastic zone [23], or the size of the plastic zone must be larger than the characteristic size of the microstructure [24]. The cracks emanating from the notches can be considered as physically short cracks. Comparison with long crack data should therefore be carried out with caution.

4.3. Assessment of the vacuum level in the internal notches

Yoshinaka et al. [25], have studied the propagation of cracks whose sizes are close to the ones studied in this work but applying a significantly higher stress. Their data obtained in air fits very well with the specimen with the surface notch. However the data obtained for the internal cracks in this work fall above the curve they obtained. This led us to question the vacuum level obtained in the artificial notches. As detailed below three strategies were employed.

4.3.1. Welding under argon

First, instead of welding the two sheets using primary vacuum, Ar gas was inserted in the chamber. The effects of this inert gas on fatigue crack propagation in Ti-6Al-4V are still poorly understood. On the one hand, Wanhill [26] studied the effect of this gas during tests under dry argon for different materials: Ti-6Al-4V and an IMI 318 (of the same chemical composition) produced in the form of sheets. The textures of these anisotropic sheets were equivalent, however the grain size in Ti-6Al-4V was twice as small. Several tests in different loading directions (to study the influence of texture) were performed. While all cracking tests led to lower propagation rates under argon than under air, notable differences were observed in the behavior of the different materials/stress directions, especially under low SIF values. Wanhill attributed these differences to the role of the propagation regime (short crack *versus* long crack) on the sensitivity to the environment (dry argon). Cracking tests carried out by Bache et al. [27] under low argon pressure (13 Pa) also showed a small decrease in propagation rates of long cracks compared to tests under air.

On the other hand, Yoshinaka et al., showed that short crack growth could be affected by an inert environment such as argon [25]. An analysis based on crack growth rates and grain-scale fracture surfaces showed that short cracks propagating in argon behaved as if they propagate (i) in air for low SIF and (ii) in vacuum for high SIF. This paradoxical behavior was not completely explained.

In this work, it can be seen in Fig. 4 that the two samples produced using argon showed the same fatigue lives (at two different stress levels) as the ones produced under vacuum.

4.3.2. Supplementary heat treatment

The second strategy used to test the vacuum level within the notch was to perform a supplementary heat treatment to evacuate remaining traces of gazes (especially Oxygen). The 3D images of the internal defects allow an estimation of the volume of air present in the notch. Assuming that the air is composed of 21.95% O_2 molecules and that it is trapped at room temperature and atmospheric pressure in the defect (limiting case), the number of O_2 molecules present in the notch before SPS could be estimated at $8.9.10^{11}$ (assuming a perfect gaz behavior at room temperature). A linear extrapolation of the experimental Ti-6Al-4V oxidation tests at 750 °C from *Guleryuz and Cimenoglu* [28] for the holding time of 5 h was performed. They determined the mass uptake of the oxide layer per unit area of Ti-6Al-4V at 750 °C with a constant air flow. Knowing the area of the laser notch, it was estimated that $5.0.10^{16}$ molecules of oxygen could have potentially left the notch to form an oxidized layer. This value is almost five orders of magnitude larger than the amount of O_2 available. It seems probable, therefore, to assume that after the supplementary heat treatment the notch has been emptied from any trace of oxygen and can be, therefore, considered under vacuum.

Once again it can be seen in Fig. 4 that the sample submitted to the supplementary heat treatment showed the same fatigue life as the ones produced by SPS under vacuum.

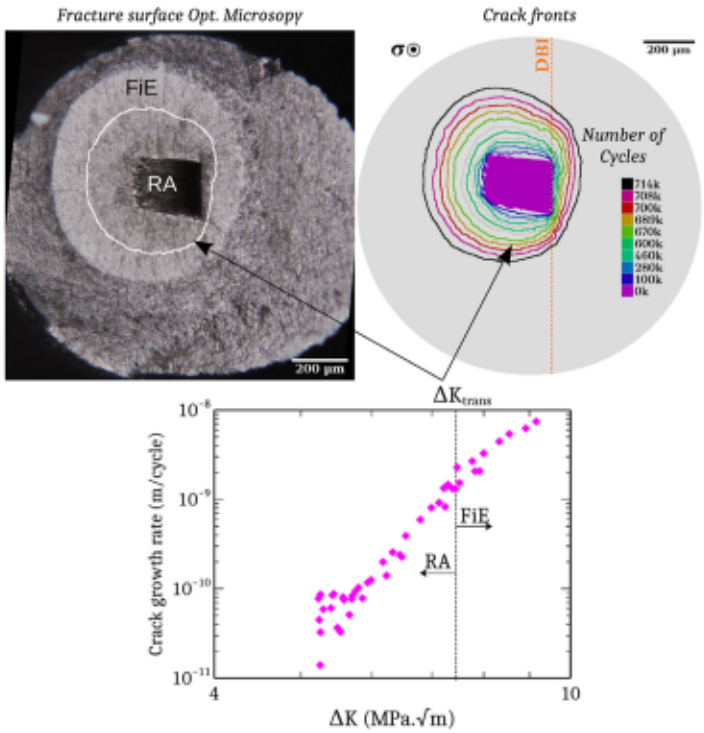

Fig. 10. Example of quantitative analysis of crack growth rates within the RA and the FIE region for sample C2. The transition between the two region is determined by combining optical inspection of the fracture surface and 3D crack fronts obtained from tomography. For this sample the transition occurs at $\Delta K_{trans.RA \longrightarrow FiE}$.

4.3.3. Samples with chimney

For comparing the propagation rate of cracks emanating from notches in air and in vacuum, a sample with a surface notch has been produced. As expected the crack growth rate in this case was much higher than those measured with the internal notches. However, one could argue that the loading conditions of these cracks are not completely identical. For example shallow surface cracks propagate close to the surface of the specimen, where plane stress conditions prevail while internal cracks might be submitted to plane strain. The conditions of plane stresses and plane strains can potentially lead to different closure levels through the plastic zone size they induce. To solve this problem, a chimney was machined by femtosecond laser to allow the internal notch to be into contact with the laboratory air.

Two samples with chimney were cycled. Their normalized lifetimes as well as those of the specimens with surface defects are reported in Fig. 4. This figure shows a strong reduction of fatigue life for the specimens having a crack propagating in air. Moreover, a clear distinction can be made between specimens with surface defects and those with chimneys indicating an effect of the crack location, probably through closure. From all these experimental data one can conclude that the method used to produce the specimens with internal notches allows us to reproduce the propagation behavior of internal fatigue cracks propagating under vacuum.

One remaining question is the variability between the da/dN curves of cracks propagating from internal notches that can be seen on Fig. 5 and which cannot be completely accounted for by experimental uncertainty. If the vacuum level can be excluded, as demonstrated above, the fact that samples have been imaged at the synchrotron under maximum load could have induced some fatigue-dwell mechanisms. The tomography scans lasted only a few minutes and were performed at room temperature, precisely the conditions which are known to alter significantly the fatigue life of Ti alloys [29]. Such effects are closely related to the local crystallography encountered by the growing crack and might induce some variability between samples. Further experiments would however be needed to verify this assumption. By using a smaller voxel size it would be possible to reduce the load on the sample during tomography. Performing shorter scans (below the minute) could also be attempted along with optimizing imaging conditions.

4.4. Crack propagation in the fish eye region

One final and important result brought by the experiments described here is that we were able to visualize and quantify crack propagation in the different zones of the fish eye region as explained in what follows.

According to the literature, in Ti-6Al-4V, after initiation (most often on a basal crystallographic plane), the propagation of an internal crack occurs in three regimes, schematically represented in Fig. 6(a) [8]. First, a short crack propagates and forms a zone called "Rough Area" (RA). In this region, the crack interacts strongly with the microstructure leading to a high roughness. Then, as the crack becomes longer, the crack path becomes more planar leading to the so-called fish eye (FiE). Two scenarios can then occur depending on where initiation happened within the section. Final fracture can occur directly from the FiE (as in Fig. 6 a)) or a third region of stable crack growth can also be observed [8].

In Fig. 6, it is possible to distinguish a first propagation zone which appears darker, and which resembles the RA region. Then, a relatively flat region, appearing lighter under the optical microscope corresponds to the FiE. In this work, the specimens containing internal notches broke immediately after the FiE zone. The transition zone between the RA and the FiE can be difficult to evaluate, optical microscopy being the best option, because of its global scale and its sensitivity to roughness. This transition was evaluated for six specimens. The transition occurred at an average value of $\Delta K_{trans.RA \longrightarrow FiE} = 9.14 \pm 1.19$ MPa $\cdot \sqrt{\text{m}}$. An example of such a measurement compared to propagation data is shown in Fig. 10. This figure also shows da/dN data obtained in the RA and in the FiE. To the best of our knowledge this is the first time that this type of data is obtained.

In the literature, Yoshinaka et al. [25] measured a value at the RA to FiE transition of 9.1 MPa $\cdot \sqrt{\text{m}}$ for short surface cracks propagating

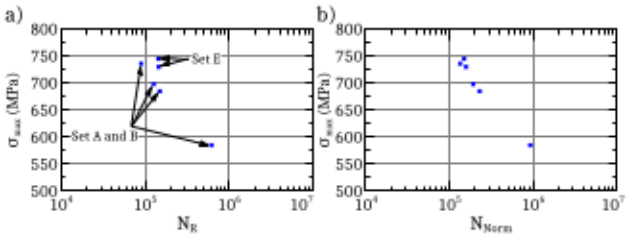

Fig. A.11. S–N curves for the ex situ fatigue tests: (a) without normalization and (b) with normalization by the initial defect size (Eq. (A.3)). Three sets of plates (A, B and E) were used to produce the specimens. The notch sizes were similar in A and B and slightly larger than in E.

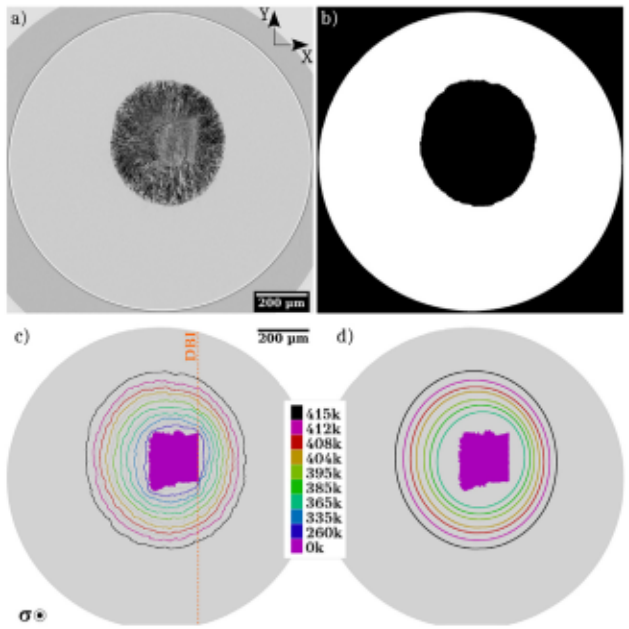

Fig. B.12. Tomographic image processing procedure. (a) Projected image of the crack of specimen A3 at 400 kcycles. (b) Corresponding segmentation. (c) Superposition of all crack fronts observed for specimen A3. (d) fitted ellipses.

under Ultra High Vacuum for a bimodal Ti-6Al-4V with a grain size of about 10 µm. In the case of internal cracks, it is generally accepted that this transition occurs at a constant ΔK whatever the applied load, as shown by Heinz and Eifler who evaluated this transition at 6.36 ± 0.39 MPa$\cdot\sqrt{\text{m}}$ [30]. A value ranging between 7 and 9 MPa$\cdot\sqrt{\text{m}}$ is quoted by Cao and Ravi Chandran [31]. At 100 Hz for load ratios R ranging from −0.3 to 0.5, Li et al. measured a value of 7.16 MPa$\cdot\sqrt{\text{m}}$ at R = 0.1 [32]. Our experimental value for $\Delta K_{trans.RA \longrightarrow FiE}$ is therefore in good agreement with literature.

Finally, at the transition, the value of the reverse plastic zone size is found equal to 3 ± 1 µm a value close to the grain size of our material, in agreement with the findings of Beevers [24]. In spite of the fact that our internal cracks initiate from relatively large defects the transition between the two cracking regimes appears to be due to plastic activity at the crack tip.

5. Conclusion

Ti-6Al-4V fatigue specimens containing a controlled internal defect were fabricated by femtosecond laser machining and diffusion bonding. Using this method, internal crack propagation was followed by synchrotron X-ray tomography for six specimens. In total, twenty specimens were tested under different conditions (environment, position of the defect).

During the fatigue tests, a very fast initiation of cracks was observed, allowing to approximate the lifetime of the specimens to the crack propagation phase.

Initiation systematically occurred in the same zone on the introduced artificial defect. A detailed analysis of the fracture surfaces showed that cleavage and near-cleavage mechanisms took place.

The propagation of internal cracks has been analyzed. First, the effect of the environment at the crack tip was studied. It was shown by various means that the internal cracks studied propagated in vacuum. A central hole was machined along the specimen axis allowing air to access the tip of the internal fatigue crack. By doing this the fatigue lives of the samples were reduced by a factor 20 because of faster crack propagation.

The observed internal cracks appeared to propagate in two distinct propagation regimes: the *Rough Area* RA and the *Fish Eye* FiE. Optical microscopy observations of the fracture surfaces allowed us to evaluate the transition between these two regimes for a constant stress intensity factor $\Delta K_{trans.RA \longrightarrow FiE} = 9.14 \pm 1.19$ MPa$\cdot\sqrt{\text{m}}$. Thus, it appears that the transition from a microstructure-influenced crack to a long crack occurs when the size of the plastic zone at the crack tip is equivalent to the grain size.

Declaration of competing interest

The authors declare that they have no known competing financial interests or personal relationships that could have appeared to influence the work reported in this paper.

Data availability

Data will be made available on request.

Acknowledgments

This work was funded by the French National Research Agency, France (GIGADEF ANR project, grant number ANR-16-CE08-0039). We acknowledge the European Synchrotron Radiation Facility for provision of beamtime at beamline ID19. The authors express their gratitude to F. Mercier for his valuable assistance for SPS diffusion bonding.

Appendix A. Normalisation of S–N curves

Internal notches have been produced in different batches leading to notch sizes which ranged from 150 to 240 µm, and inducing a difference in the initial crack size a_i of the order of 25%. In order to compare the fatigue life of the samples with internal defects, this effect must be taken into account. A normalization of the fatigue life has been performed as described in what follows.

It is known from tomography that crack initiation occurs within less than 10% of the fatigue life. The latter can therefore be estimated using the Paris law obtained for cracks propagating in vacuum (Eq. (3)) from an initial length a_i to a final length a_f.

Assuming a formulation of the SIF in the form of:

$$K = \beta\sigma\sqrt{\pi a} \tag{A.1}$$

where β is the usual shape factor, σ the applied stress and a the crack size, the fatigue life of a sample containing an internal defect can be estimated as follows:

$$N_R = \frac{1}{(1-\frac{m}{2})\beta^m \Delta\sigma^m \pi^{m/2}} \int_{a_i}^{a_f} \frac{da}{a^{m/2}}$$

$$= \frac{1}{(1-\frac{m}{2})\beta^m \Delta\sigma^m \pi^{m/2}} \left[\frac{1}{a_f^{\frac{m}{2}-1}} - \frac{1}{a_i^{\frac{m}{2}-1}} \right]$$

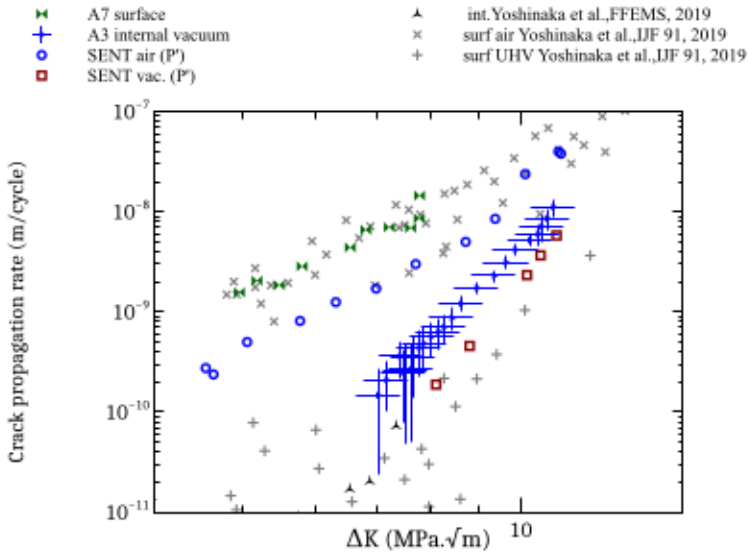

Fig. B.13. Experimental error for sample A3.

With $a_f \gg a_i$ this equation can be simplified as:

$$N_R \propto \frac{1}{a_i^{\frac{m}{2}-1}} = N_{Approx}(a_i) \tag{A.2}$$

This formula (A.2) was used to normalize the fatigue lives of the samples cycled in the laboratory. The value of the slope m is taken equal to 11.43, which agrees well with our experimental data. The specimen with the smallest artificial defect was chosen as the reference for normalization. Noting a_{ref} the crack size equivalent to the smallest defect, the normalized life N_{Norm} of a specimen with a fatigue life N_R and an initial equivalent crack size a_i writes:

$$N_{Norm}(a_i) = N_R \frac{N_{Approx}(a_{ref})}{N_{Approx}(a_i)} = N_R \frac{a_i^{\frac{m}{2}-1}}{a_{ref}^{\frac{m}{2}-1}} \tag{A.3}$$

The influence of this normalization on the SN curves is shown in Fig. A.11. In this example, specimens from three different batches A, B and E were used. The first two sets had defects of identical size while the last one contained smaller defects. After normalization, it can be seen that the scatter in the results almost disappears.

Appendix B. Quantification of crack growth rate form 3D images and uncertainty calculation

In total seven specimens have been cycled in situ at the synchrotron leading to more than 150 3D images to analyze. The procedure to extract semi automatically crack fronts from this large dataset is described in what follows.

1. For each crack propagation stage investigated, projection along $\vec{z}$ (parallel to the loading axis) of the minimum value of the voxel gray levels in the reconstructed volume using the Z-project function of the ImageJ software [9] (Fig. B.12(a))
2. registration of all images obtained in step 1
3. Segmentation of the image (gray level threshold) and extraction of the crack fronts (Fig. B.12(b) and (c))
4. Fit of the crack fronts Fig. B.12(d))).

The whole sequence is illustrated for sample A_3 in Fig. B.12.

The uncertainty in the position of the propagation curves has been estimated. To do so, one must first evaluate the uncertainty on (da/dN) and on ΔK. The cracks length a is equal to a_{eq} (5). The crack growth rate writes:

$$\left.\frac{\Delta a}{\Delta N}\right|_n = \frac{a_{n+1} - a_{n-1}}{N_{n+1} - N_{n-1}} \tag{B.1}$$

For an internal crack with a projected area equal to a circle of radius a the SIF is given by:

$$\Delta K = 0,5 \frac{F_{max} - F_{min}}{S_{sample}} \sqrt{\pi \sqrt{\pi a^2}} \tag{B.2}$$

The uncertainties estimated for Δa, F_{max} and F_{min} at each cycle and for the sample section S_{sample} are given in Table B.3.

The error propagation calculation for ($\Delta a/\Delta N$ and ΔK) is computed using the following formula:

$$\Delta f(x_j) = \sqrt{\sum_j \left[\left(\frac{\partial f}{\partial x_j} \right)^2 \Delta x_j^2 \right]} \tag{B.3}$$

Where f is the considered variable ($\Delta a/\Delta N$ or ΔK) and x_j all the variables used for calculating f and for which with an experimental error has been estimated.

The result of this calculation is shown in Fig. B.13 for sample A3. The error on da/dN values is small except when the crack has a very short size. The error on ΔK is larger but remains constant when the crack propagates. Overall, for the experimental conditions investigated, the error level remains acceptable and allows to compare crack growth data for various environment.

Table B.3
Measurement uncertainties taken into account for the calculations. The error on the forces was evaluated at twice the error indicated by the manufacturer of the sensor used. The errors related to the cross-sectional area of the specimen and the crack length are more subjective. The values taken into account were considered as maximum errors.

Δa	ΔF_{max}	ΔF_{min}	ΔS_{sample}
3 pixels (2,16 µm)	20 N	20 N	0,04 mm^2

References

[1] BEA. Accident to the AIRBUS A380-861 registered F-HPJE and operated by Air France on 30/09/2017 en route over Greenland [Investigation delegated to BEA by the authorities of Denmark]. Rapport d'enquête, Bureau d'Enquêtes et d'Analyse pour la Sécurité de l'Aviation civile; 2020, URL: https://www.bea.aero/en/investigation-reports/notified-events/detail/event/accident-to-the-airbus-a380-registered-f-hpje-and-operated-by-air-france-on-30092017-en-route-over/.

[2] Klinger C, Bettge D. Eng Fail Anal 2013;35:66–81. http://dx.doi.org/10.1016/j.engfailanal.2012.11.008, URL: http://www.sciencedirect.com/science/article/pii/S1350630712002543.

[3] Wu SC, Xiao TQ, Withers PJ. 2017;182:127–56. http://dx.doi.org/10.1016/j.engfracmech.2017.07.027, URL: http://www.sciencedirect.com/science/article/pii/S0013794417305052,

[4] Chapman TP, Kareh KM, Knop M, Connolley T, Lee PD, Azeem MA, et al. Acta Mater 2015;99:49–62. http://dx.doi.org/10.1016/j.actamat.2015.07.069, URL: http://www.sciencedirect.com/science/article/pii/S1359645415005558.

[5] Naragani D, Sangid MD, Shade PA, Schuren JC, Sharma H, Park J-S, et al. Acta Mater 2017;137:71–84. http://dx.doi.org/10.1016/j.actamat.2017.07.027, URL: http://www.sciencedirect.com/science/article/pii/S1359645417305888.

[6] Yoshinaka F, Nakamura T, Takeuchi A, Uesugi M, Uesugi K. Fatigue Fract Eng Mater Struct 2019;1–13. http://dx.doi.org/10.1111/ffe.13085, URL: http://onlinelibrary.wiley.com/doi/abs/10.1111/ffe.13085.

[7] Junet A, Messager A, Boulnat X, Weck A, Boller E, Helfen L, et al. Scr Mater 2019;171:87–91. http://dx.doi.org/10.1016/j.scriptamat.2019.05.018, URL: http://www.sciencedirect.com/science/article/pii/S1359646219302866.

[8] Hong Y, Sun C. Theor Appl Fract Mech 2017;92:331–50.

[9] Junet A. Etude tridimensionnelle de la propagation en fatigue de fissures internes dans les matériaux métalliques (Ph.D. thesis), Lyon, INSA; 2021, URL: https://www.theses.fr/2021LYSEI006.

[10] Tada H, Paris PC, Irwin GR. The stress analysis of cracks handbook. 3rd ed.. ASME Press; 2000, http://dx.doi.org/10.1115/1.801535, URL: https://asmedigitalcollection.asme.org/ebooks/book/188/the-stress-analysis-of-cracks-handbook-third.

[11] Oguma H, Nakamura T. Int J Fatigue 2013;50:89–93. http://dx.doi.org/10.1016/j.ijfatigue.2012.02.012, URL: http://www.sciencedirect.com/science/article/pii/S0142112312000734.

[12] Yukitaka M, Masahiro E. Eng Fract Mech 1983;17(1):1–15. http://dx.doi.org/10.1016/0013-7944(83)90018-8, URL: http://www.sciencedirect.com/science/article/pii/0013794483900188.

[13] Evans WJ, Bache MR, McElhone M, Grabowski L. Int J Fatigue 1997;19(93):177–82. http://dx.doi.org/10.1016/S0142-1123(97)00035-2, URL: http://www.sciencedirect.com/science/article/pii/S0142112397000352.

[14] Sinha V, Mills MJ, Williams JC. Metall Mater Trans A 2006;37(6):2015–26. http://dx.doi.org/10.1007/s11661-006-0144-5, URL: http://link.springer.com/10.1007/s11661-006-0144-5.

[15] Uta E, Gey N, Bocher P, Humbert M, Gilgert J. J Microsc 2009;233(3):451–9. http://dx.doi.org/10.1111/j.1365-2818.2009.03141.x, URL: http://onlinelibrary.wiley.com/doi/abs/10.1111/j.1365-2818.2009.03141.x.

[16] Pilchak AL, Williams JC. Metall Mater Trans A 2011;42(4):1000–27. http://dx.doi.org/10.1007/s11661-010-0507-9, URL: https://doi.org/10.1007/s11661-010-0507-9.

[17] Pilchak AL, Bhattacharjee A, Rosenberger AH, Williams JC. Int J Fatigue 2009;31(5):989–94. http://dx.doi.org/10.1016/j.ijfatigue.2008.03.036, URL: http://www.sciencedirect.com/science/article/pii/S0142112308001035.

[18] Stroh AN. Adv Phys 1957;6(24):418–65. http://dx.doi.org/10.1080/00018735700101406, URL: https://doi.org/10.1080/00018735700101406.

[19] Evans WJ, Bache MR. Int J Fatigue 1994;16(7):443–52. http://dx.doi.org/10.1016/0142-1123(94)90194-5, URL: http://www.sciencedirect.com/science/article/pii/0142112394901945.

[20] Dunne FPE, Rugg D. Fatigue Fract Eng Mater Struct 2008;31(11):949–58. http://dx.doi.org/10.1111/j.1460-2695.2008.01284.x, URL: http://onlinelibrary.wiley.com/doi/abs/10.1111/j.1460-2695.2008.01284.x.

[21] Bache MR, Dunne FPE, Madrigal C. J Strain Anal Eng Des 2010;45(5):391–9. http://dx.doi.org/10.1243/03093247JSA594, URL: https://doi.org/10.1243/03093247JSA594.

[22] Jones IP, Hutchinson WB. Acta Metall 1981;29(6):951–68. http://dx.doi.org/10.1016/0001-6160(81)90049-3, URL: http://www.sciencedirect.com/science/article/pii/0001616081900493.

[23] Krupp U. Fatigue crack propagation in metals and alloys: Microstructural aspects and modelling concepts. John Wiley & Sons; 2007.

[24] Beevers CJ. Met Sci 1977;11(8–9):362–7. http://dx.doi.org/10.1179/msc.1977.11.8-9.362, URL: https://doi.org/10.1179/msc.1977.11.8-9.362.

[25] Yoshinaka F, Nakamura T, Takaku K. Int J Fatigue 2016;91:29–38. http://dx.doi.org/10.1016/j.ijfatigue.2016.05.024, URL: http://www.sciencedirect.com/science/article/pii/S0142112316301268.

[26] Wanhill RJH. Metall Trans A 1976;7(9):1365–73. http://dx.doi.org/10.1007/BF02658822, URL: https://doi.org/10.1007/BF02658822.

[27] Bache MR, Evans WJ, McElhone M. Mater Sci Eng A 1997;234–236:918–22. http://dx.doi.org/10.1016/S0921-5093(97)00402-4, URL: http://www.sciencedirect.com/science/article/pii/S0921509397004024.

[28] Guleryuz H, Cimenoglu H. J Alloys Compd 2009;472(1):241–6. http://dx.doi.org/10.1016/j.jallcom.2008.04.024, URL: http://www.sciencedirect.com/science/article/pii/S0925838808006609.

[29] Dichtl C, Lunt D, Atkinson M, Thomas R, Plowman A, Barzdajn B, et al. 2022;229:117691. http://dx.doi.org/10.1016/j.actamat.2022.117691, URL: https://www.sciencedirect.com/science/article/pii/S1359645422000787.

[30] Heinz S, Eifler D. Int J Fatigue 2016;93:301–8. http://dx.doi.org/10.1016/j.ijfatigue.2016.04.026, URL: http://www.sciencedirect.com/science/article/pii/S0142112316300809.

[31] Cao F, Ravi Chandran KS. Int J Fatigue 2017;102:48–58. http://dx.doi.org/10.1016/j.ijfatigue.2017.05.004, URL: http://www.sciencedirect.com/science/article/pii/S0142112317302086.

[32] Li W, Zhao H, Nehila A, Zhang Z, Sakai T. Int J Fatigue 2017;104:342–54. http://dx.doi.org/10.1016/j.ijfatigue.2017.08.004, URL: http://www.sciencedirect.com/science/article/pii/S0142112317303341.